nature research https://doi.org/10.1038/s41565-020-0773-7

Supplementary information

Dirac-vortex topological cavities

In the format provided by the authors and unedited

Supplementary Information for "Dirac-vortex topological cavities"

Xiaomei Gao[†], Lechen Yang[†], Hao Lin, Lang Zhang,
Jiafang Li, Fang Bo, Zhong Wang, and Ling Lu[*]

Abstract

CONTENTS

[*] linglu@iphy.ac.cn. [†]The first two authors contributed equally.

A. TOPOLOGICAL UNDERSTANDING OF DFB AND VCSEL

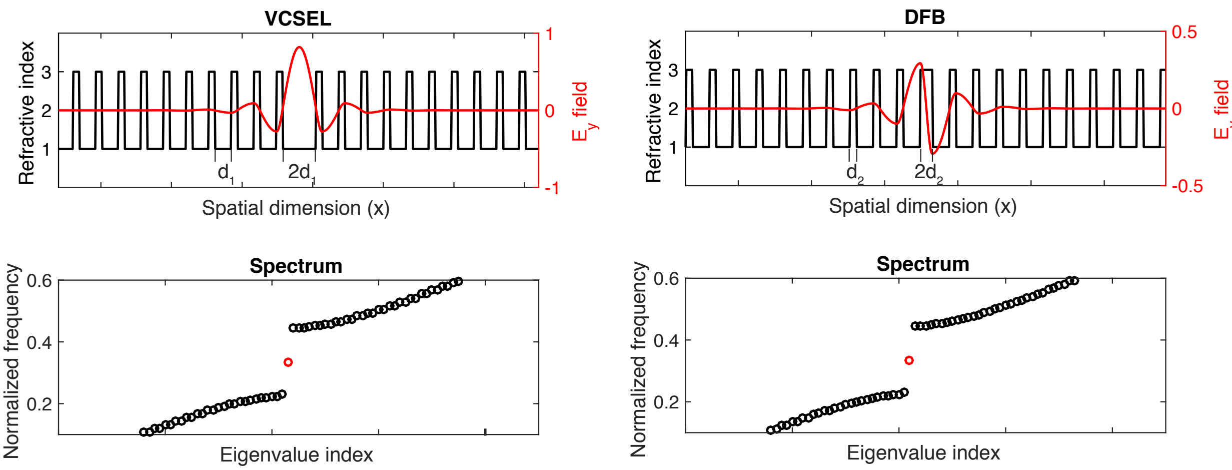

FIG. S1. Mid-gap modes in VCSEL and DFB. Here the refractive index contrast is magnified, from that in real devices, to better illustrate the topological feature (that the topological mode is localized spatially at the kink and spectrally at the middle of the gap). In both simulations, the 1D layers are quarter-wavelength stacks and the central defect layers have an optical path of half wavelength (phase of π). This π phase is the reason for the anti-phase resonant condition at Bragg frequency and also the reason for the difference of π Berry phase of the bulk lattices on the two sides of the kink. One example of VCSEL layers can be found in the following book (Physics of Photonic Devices, 2nd Edition, Shun Lien Chuang, Chapter 11, Page 506, Figure 11.13.)

B. FSR IMPROVEMENTS

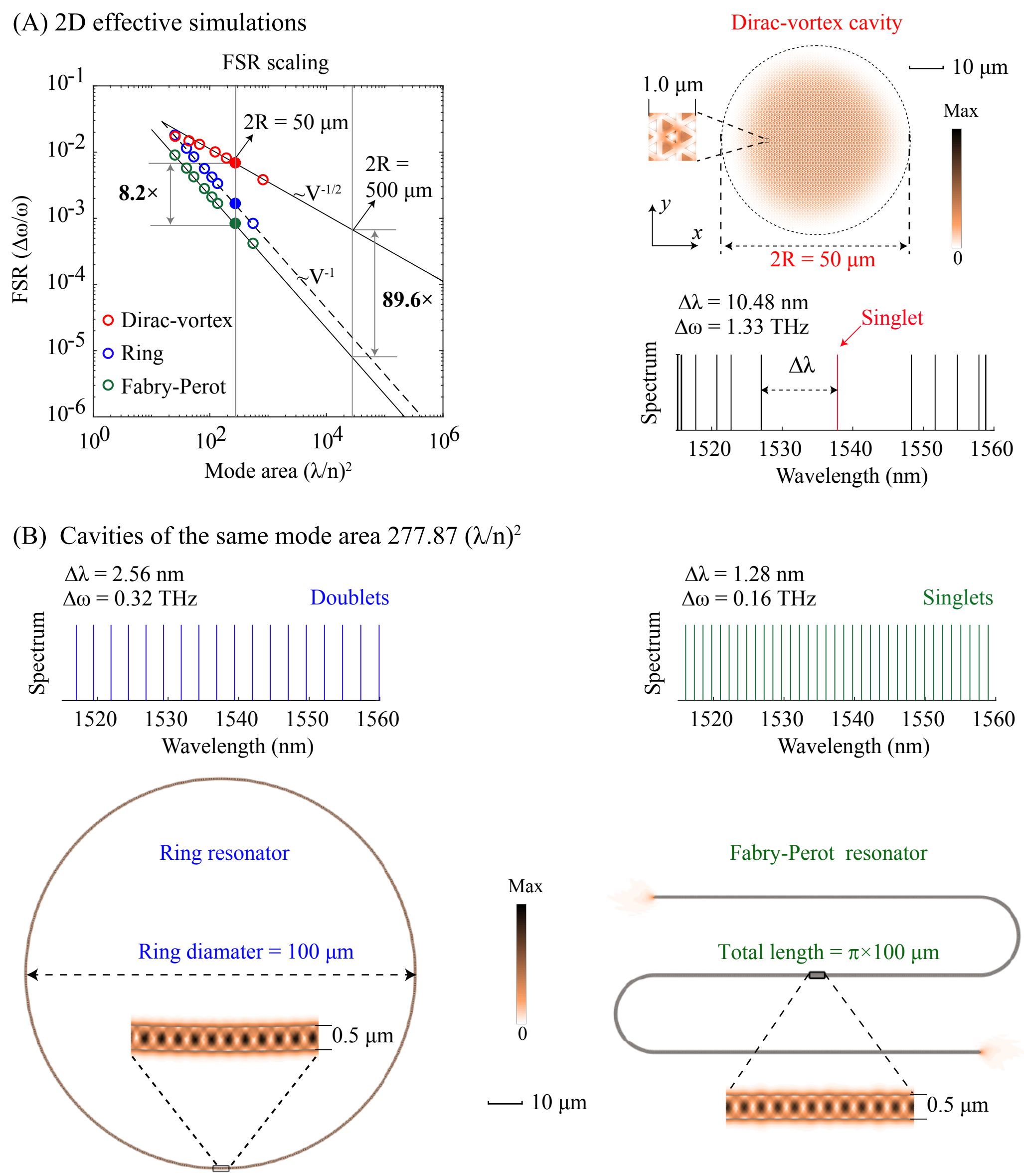

FIG. S2. We investigate the FSR improvements of the Dirac-vortex cavity versus the regular ring and Fabry-Perot resonators on SOI and at $1.55\mu m$ wavelength, using effective 2D simulations (refractive index of 2.6 and 1). The modes in a ring resonator are doubly degenerate (CW and CCW modes) and its FSR is twice of that of the singly-degenerate Fabry-Perot resonator with the same length. We compare the single-mode Dirac-vortex cavity with the Fabry-Perot resonators of the the same area (volume). The Dirac-vortex FSR, vortex diameter of $50\mu m$, is 8.2 times larger than that of the Fabry-Perot and is 89.6 times larger if the vortex diameter is $500\mu m$. Overall, the FSR of a Dirac-vortex is one to two order of magnitudes larger than that of conventional cavities of the same mode volume.

C. $\mathbf{k}\cdot\mathbf{p}$ HAMILTONIAN

Symmetry		$H(\boldsymbol{k})$	$\sigma_x k_x \tau_z$	$\sigma_z k_y \tau_z$	$m_1 \tau_x$	$m_2 \tau_y$	$m' \sigma_y \tau_z$
$[H$,Sym.$]$=0	Time reversal	$\mathcal{T} = \tau_x K\|_{\boldsymbol{k}\to-\boldsymbol{k}}$	$\surd$	$\surd$	$\surd$	$\surd$	$\surd$
	Parity/Inversion	$\mathcal{P} = \tau_x\|_{\boldsymbol{k}\to-\boldsymbol{k}}$	$\surd$	$\surd$	$\surd$	$\times$	$\times$
	Parity-Time	$\mathcal{PT} = K$	$\surd$	$\surd$	$\surd$	$\times$	$\times$
$\{H$,Sym.$\}$=0	Particle-hole/Charge-conjugation	$\mathcal{C} = \sigma_y \tau_y K\|_{\boldsymbol{k}\to-\boldsymbol{k}}$	$\surd$	$\surd$	$\surd$	$\surd$	$\times$
	Chiral	$\mathcal{S} = \mathcal{TC} = \sigma_y \tau_z$	$\surd$	$\surd$	$\surd$	$\surd$	$\times$

TABLE S1. Symmetry analysis of the 2D Bosonic Dirac Hamiltonian (H) of four bands. Chiral symmetry ($\mathcal{S}$) is the protecting symmetry. K is the complex conjugation. $|_{\boldsymbol{k}\to-\boldsymbol{k}}$ represents the momentum flip. $\surd$ and $\times$ are used to indicate whether a term in Hamiltonian is invariant under each symmetry or not. τ_i and σ_i are both Pauli matrices. [] and $\{\}$ are commutator and anti-commutator.

D. CHOICE OF CAVITY CENTER FOR C_{3v} SYMMETRY

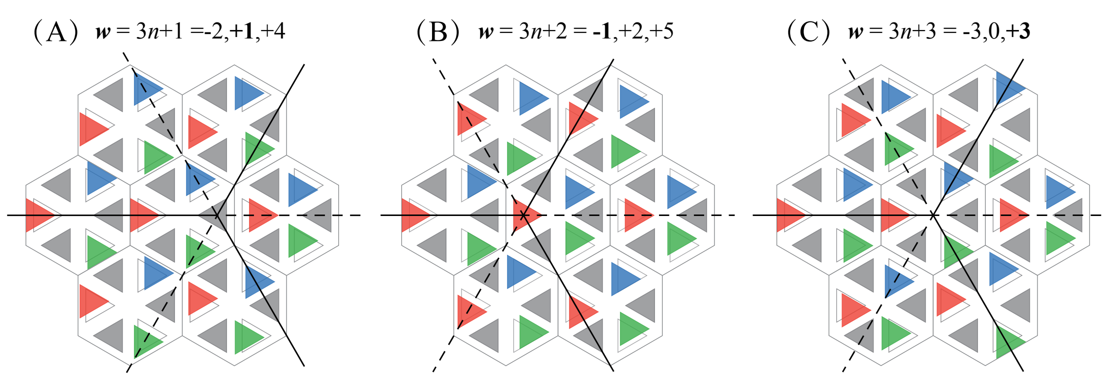

FIG. S3. A total of three different choices for cavity centers to keep the cavity C_{3v} symmetric for all winding numbers (w). The gray triangle is the stationary sub-lattice. The three triangles of the shifted sub-lattice in each supercell are colored by their initial relative phase ϕ_0 (the direction of the shift). The vortex size is $R = 0a$ for the three examples with winding numbers of $w = +1$, $w = -1$ and $w = +3$.

Only the central seven super-cells are illustrated.

E. NEGATIVE WINDING NUMBERS

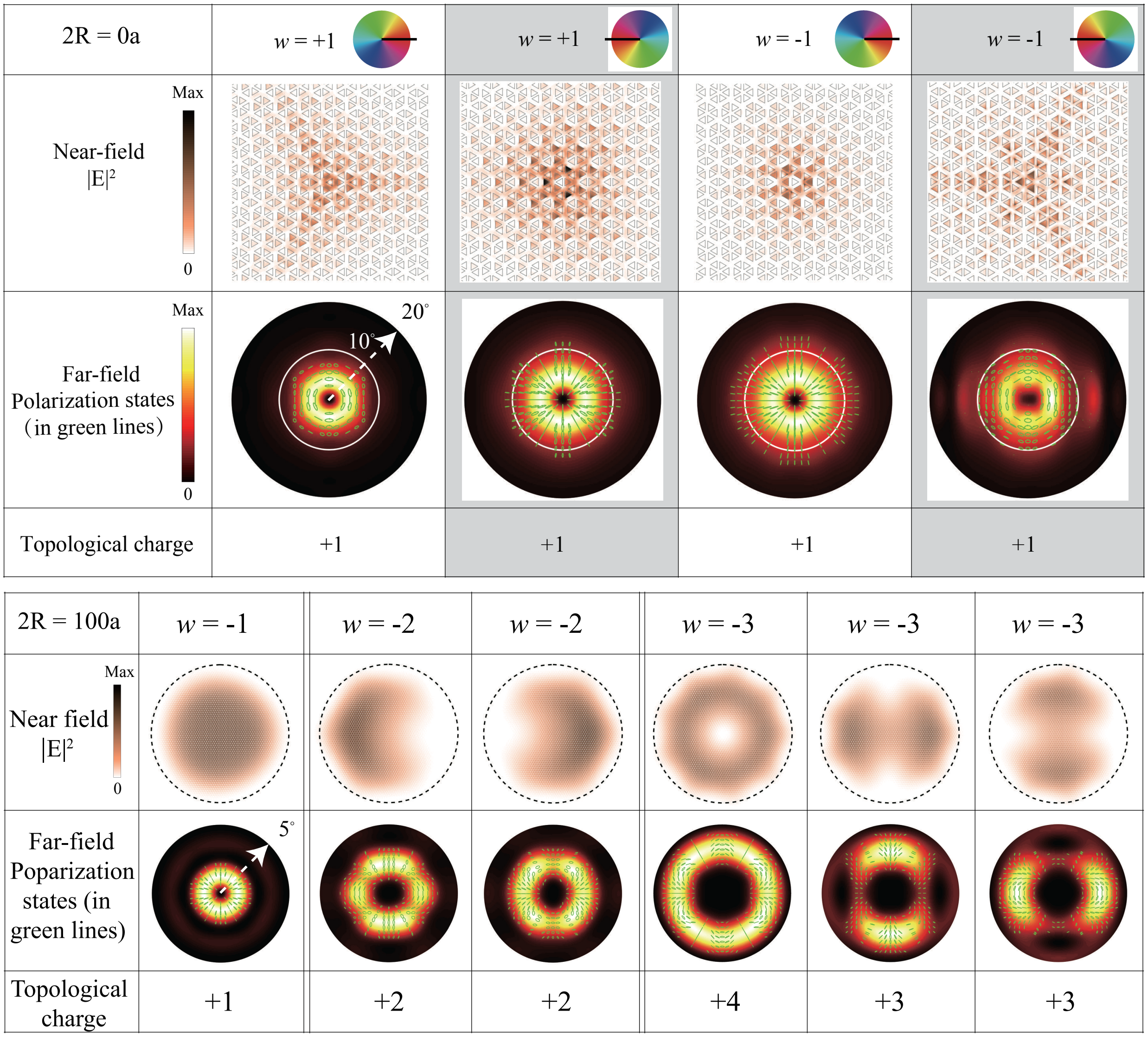

FIG. S4. TOP: Comparison between positive and negative winding numbers of the Dirac vortex cavities ($2R = 0a$). In all four cases, we choose the cavity centers so that the cavities are C_{3v} symmetric. We also provide vortices with $-x$ axes as the zero-phase reference line in gray background. All four cavities, of opposite winding numbers and different reference phase angles, are not symmetry related structures in our design. The field energy peaks at different sub-lattices (triangles pointing to the right or left) of the honeycomb lattice for opposite winding numbers. BOTTOM: Negative winding numbers of $w = -1, -2, -3$ and $2R = 100a$.

F. PURCELL FACTOR

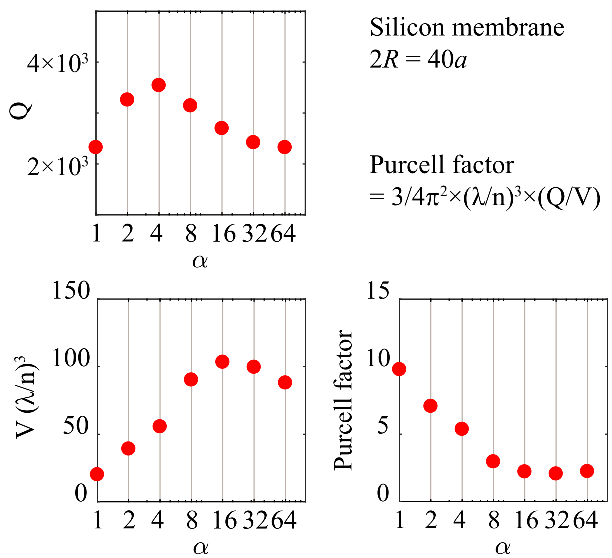

FIG. S5. The dependance of Q, V and Q/V (Purcell factor) on the shape factor α of the vortex cavity by 3D FDTD. As can be seen from the low Purcell factor, this cavity is not designed to enhance spontaneous emission in the first place.

G. CONSTANT MODE FREQUENCY

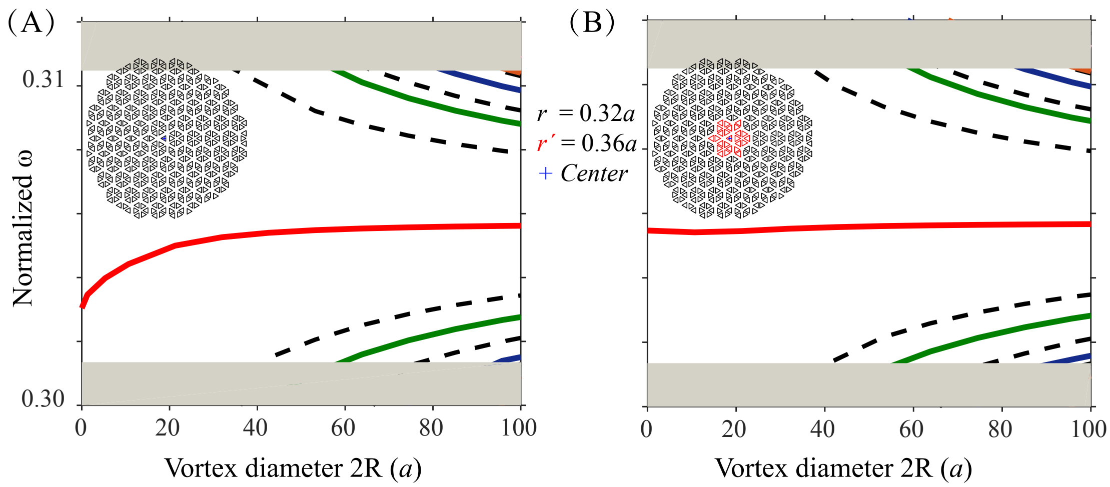

FIG. S6. Fine-tuning the central air-holes so that the cavity frequency is nearly independent of vortex size ($\alpha = 4$). In the large cavity limit, the cavity resonates at the Dirac frequency, because the cavity mode experiences large areas of the unperturbed Dirac lattice at the centeral area of the vortex. In the small cavity limit, the cavity mode only experiences the defect site and its frequency does not need to stay at the Dirac frequency. So, we enlarge or shrink a few central air holes to tune the frequencies of the small-cavities; this local perturbation does not affect the frequencies of the large-cavities whose modes are much more extended in area.

H. ALL CAVITY MODES

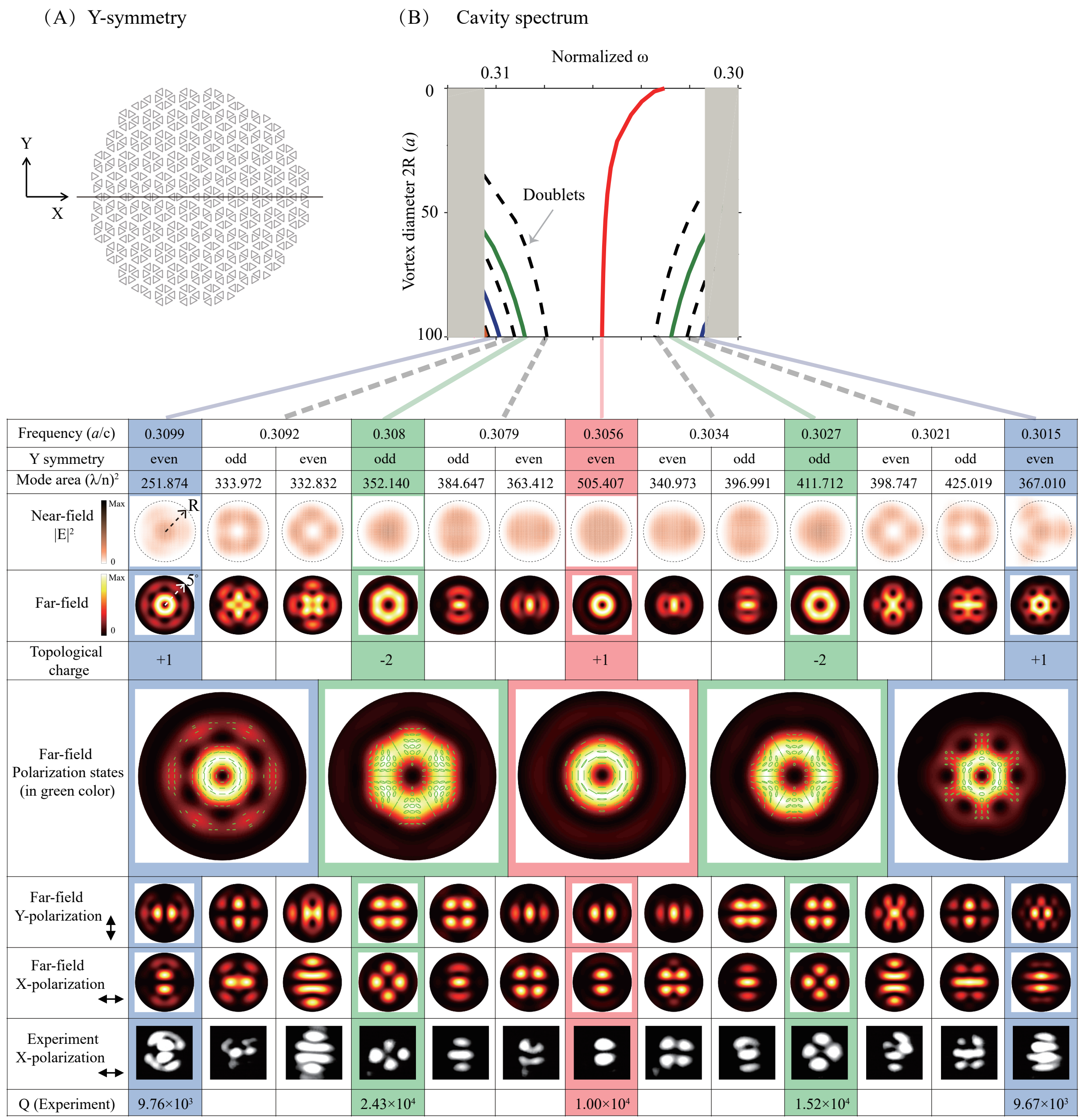

FIG. S7. Modal properties of all cavity modes ($w = +1$) from 2D simulations and experiments. The Y symmetry is determined by the H_z field. The polarization states in the far-fields are plotted in detail for the five non-degenerate modes and their experimental Q values are also listed.

I. SINGLE-LOBE BEAM WITH NON-UNIFORM PHASE WINDING

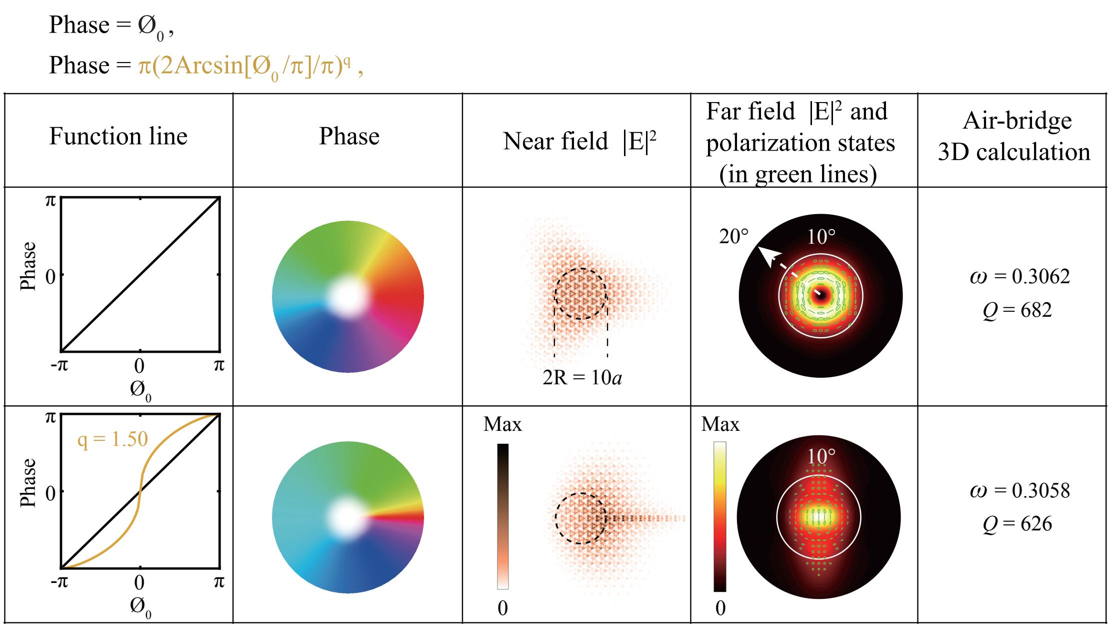

FIG. S8. The donut beam can be converted to a single-lobe beam, useful for some applications, by varying the angular distribution of the phase of the Dirac gap (mass). 3D calculations show that the Q and frequency of the cavity do not vary much due to the phase nonuniformity.

J. SUBSTRATE COMPATIBILITY (ALL SEMICONDUCTOR)

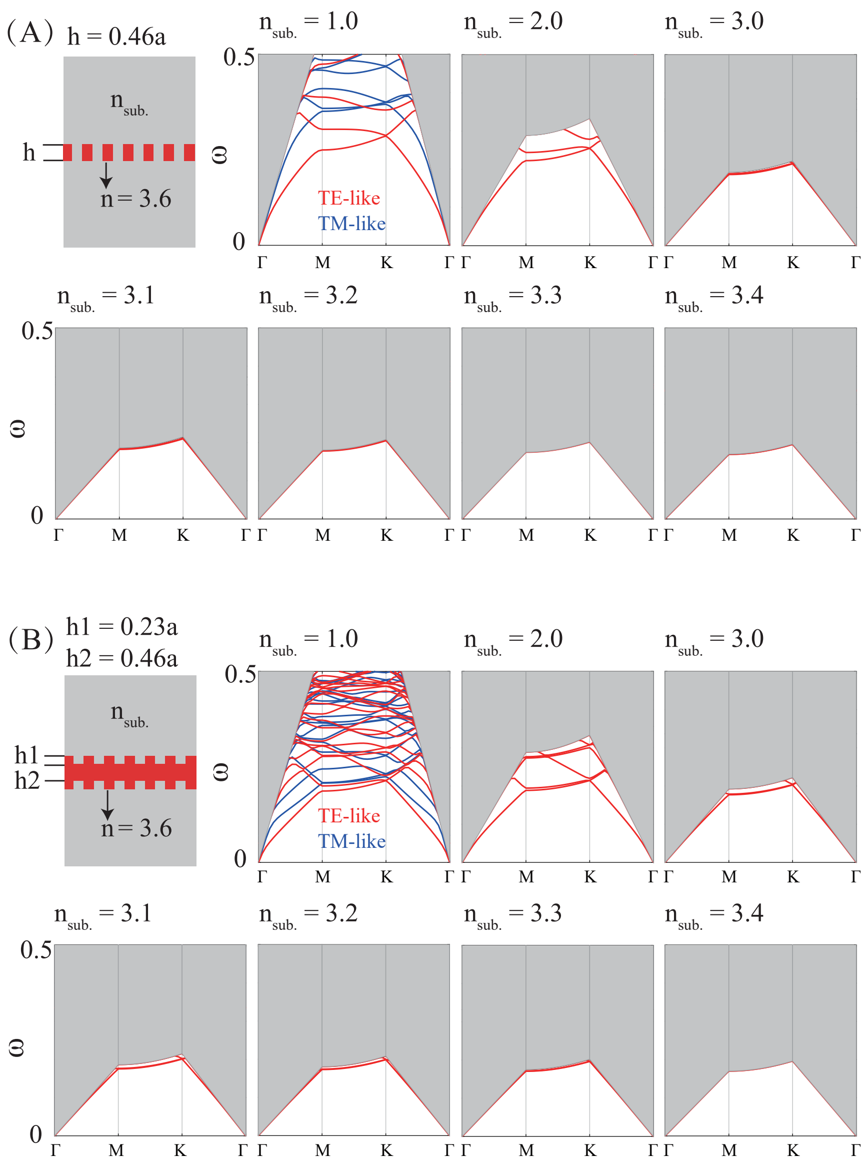

FIG. S9. Band structures of all semiconductor PCSEL designs, in which the air voids in Fig. 4 of main text are filled with substrate materials. Compared to the air-voids design, the all semiconductor design has a larger critical substrate index $n^c_{\text{sub}} \approx 3.0$ in (A) and $n^c_{\text{sub}} \approx 3.3$ in (B). TM-like modes are plotted for the $n_{\text{sub}} = 1.0$ cases only. The light cone, filled by gray color, drops as n_{sub} increases.

K. CAVITIES OF $w = +1, +2, +3$

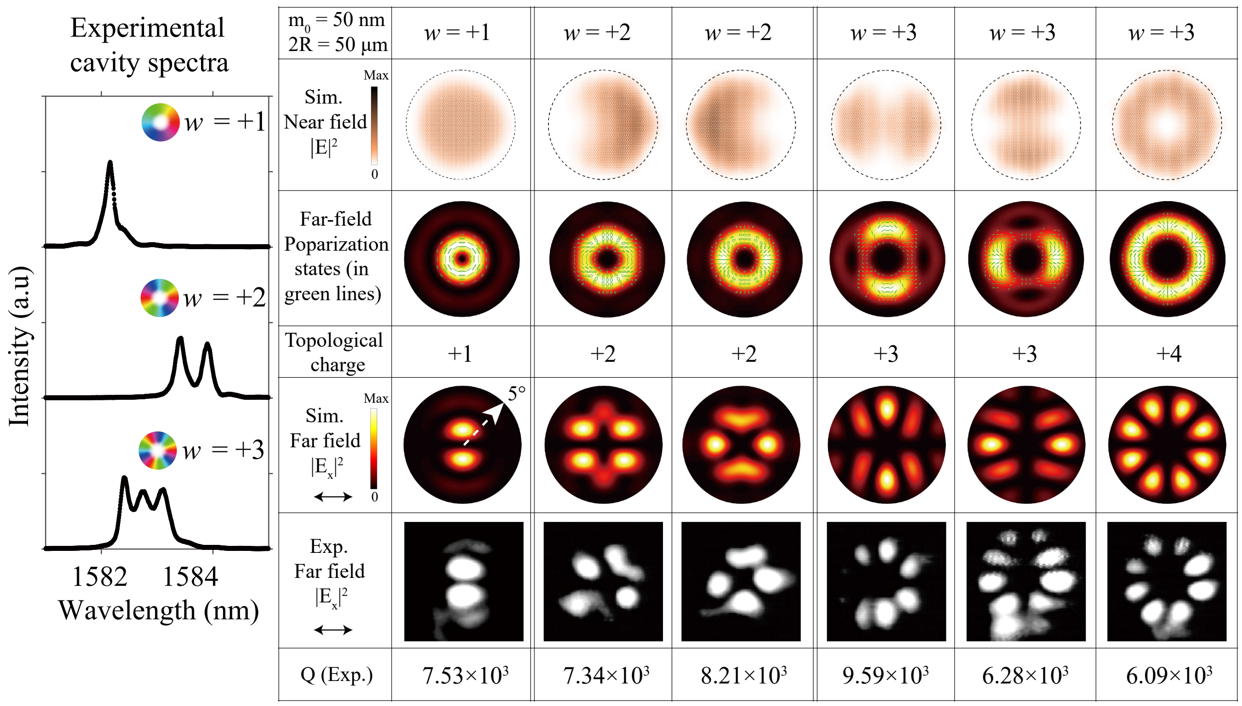

FIG. S10. Experimental and simulation results of the cavities with winding numbers $w = +1, +2, +3$ and modulation amplitude $m_0 = 50nm$. In these cases, we fixed the cavity center (see Fig. S3) so that only the $w = +1$ cavity is C_{3v} symmetric and the $w = +2, +3$ cavities have all singlet modes. Since C_{3v} has a doublet representation, so if we choose the corresponding centers to enforce $w = +2, +3$ cavities to be C_{3v} symmetric, two of the modes will be degenerate in both cases.

L. CROSS-POLARIZATION REFLECTION SETUP

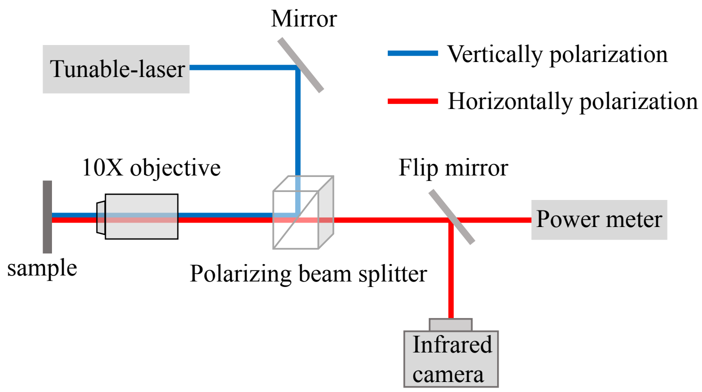

FIG. S11. Cross-polarized reflectivity measurement setup. The polarization beam splitter (PBS) is the key optical element enabling the measurement. The PBS has two functions. First, the PBS separates the pump beam and sample emission, sharing the same wavelength, by reflecting the pump beam in one polarization while passing partial sample emission containing the other polarization. Second, the transmitted beam after PBS reveals the polarization states of the cavity far fields. The number of zero-intensity radial lines on camera equals the topological charge (in magnitude) of the emitted vector beam.

M. VARY m_0 AND R IN EXPERIMENTS

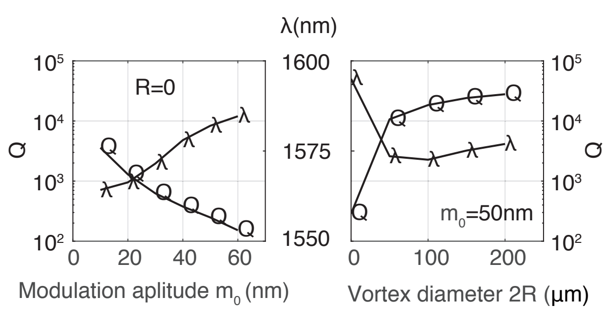

FIG. S12. The Qs and resonant wavelengths (λ) of the single-vortex ($w = +1$) cavities measured as a function of the modulation amplitude m_0 and vortex size R. In both cases, Q increases with the increase of mode area, because the mode area increases with the decrease of modulation amplitude and the increase of vortex size. For positive winding numbers, the wavelengths of small cavities are longer than the original Dirac wavelength.